PHILOSOPHICAL TRANSACTIONS A

royalsocietypublishing.org/journal/rsta

Research

Cite this article: Herman A. 2022 Granular effects in sea ice rheology in the marginal ice zone. *Phil. Trans. R. Soc. A* **380**: 20210260. https://doi.org/10.1098/rsta.2021.0260

Received: 2 March 2022
Accepted: 8 July 2022

One contribution of 17 to a theme issue 'Theory, modelling and observations of marginal ice zone dynamics: multidisciplinary perspectives and outlooks'.

Subject Areas:
oceanography, geophysics

Keywords:
sea ice, granular rheology, sea ice rheology, floe size distribution, polydispersity, marginal ice zone

Author for correspondence:
A. Herman
e-mail: agaherman@iopan.pl

Present address: Institute of Oceanology, Polish Academy of Sciences, Sopot, Poland.

THE ROYAL SOCIETY PUBLISHING

Granular effects in sea ice rheology in the marginal ice zone

A. Herman

Institute of Oceanography, University of Gdańsk, Gdańsk, Poland

AH, 0000-0001-5112-7165

Sea ice in the marginal ice zone (MIZ) consists of relatively small floes with a wide size span. In response to oceanic and atmospheric forcing, it behaves as an approximately two-dimensional, highly polydisperse granular material. The established viscous-plastic rheologies used in continuum sea ice models are not suitable for the MIZ; the collisional rheology, in which sea ice is treated as a granular gas, captures only one aspect of the granular behaviour, typical for a narrow range of conditions when dynamics is dominated by binary floe collisions. This paper reviews rheology models and concepts from research on granular materials relevant for MIZ dynamics (average stress as a result of 'microscopic' interactions of grains; $\mu(I)$ and collisional rheologies). Idealized discrete-element simulations are used to illustrate granular effects and strong influence of the floe size distribution on strain–stress relationships in sheared sea ice, demonstrating the need for an MIZ rheology model capturing the whole range of 'regimes', from quasi-static/dense flow in the inner MIZ to the inertial flow in the outer MIZ.

This article is part of the theme issue 'Theory, modelling and observations of marginal ice zone dynamics: multidisciplinary perspectives and outlooks'.

1. Introduction

Sea ice in the marginal ice zone (MIZ)—the part of the ice cover adjacent to the open ocean and influenced by its presence—typically consists of relatively small, highly mobile ice floes. Ice fragmentation is a result of

many dynamic processes, including breaking by waves, shear deformation and floe collisions, combined with thermodynamic influences, e.g. upwelling of relatively warm water masses at the ice edge. The resulting floe size distributions (FSDs) in the MIZ often are scale-invariant in the size range of relatively small floes and have exponential tails related to the existence of the upper size limit, i.e. they are well described by a tapered power law [1]. The relationship between floe size and dynamic/thermodynamic processes in the MIZ is very complex and mutual: the response of the ice to oceanic and atmospheric forcing is FSD dependent [2,3]. Granular effects in sea ice dynamics have received much attention of researchers in recent years, with several studies exploring the influence of FSDs on selected processes (e.g. eddy formation in the ocean mixed layer and ice melting rates [4]; formation of floe clusters [5,6]; size-dependent response of floes to wind/currents [7]; jamming phenomena [8]; wave energy attenuation [9,10]; and many more), or on large-scale, seasonal and long-term evolution of sea ice in polar regions (e.g. [11–15]). In spite of a substantial progress, however, many aspects of those interactions remain poorly understood [16]. As far as sea ice rheology—the main subject of this paper—is concerned, the attempts to parametrize granular effects in continuum models have been largely limited to the collisional regime, i.e. the relatively narrow range of ice concentrations where, on the one hand, the floes can move freely in open-water spaces between them, but, on the other hand, they collide with their neighbours frequently and energetically enough to produce substantial collisional stress in the ice. Not surprisingly, when the collisional rheology [17–19] is implemented in large-scale sea ice models together with the classic Hibler's viscous-plastic rheology [20], its effects are noticeable in terms of, e.g. MIZ width and compactness [14], but overall tend to be rather minor. Other continuum rheological models that aim at taking into account the discrete nature of sea ice are suitable for the dense ice pack rather than the MIZ and reproduce selected, isolated aspects of granular behaviour, e.g.dilatancy effects [21], or anisotropy [22]. At smaller scales, smoothed particle hydrodynamics and discrete-element models (DEMs) have been used to assess the suitability of the viscous-plastic rheology and Mohr–Coulomb type yield conditions to granular sea ice flow in various geometries [23–26].

In parallel with significant progress in research on sea ice dynamics at the floe scale, briefly sketched above, substantial developments have taken place in research on granular rheology, including that of dry granular materials and suspensions. One of the main goals of this study is to provide a concise—and, by necessity, rather selective—review of ideas that seem relevant for sea ice and that might inspire further research on MIZ dynamics and, in a further perspective, lead to the development of a MIZ rheology model capturing the whole range of behaviours, from quasi-static, dense flow in the inner MIZ to dilute, inertial flow close to the ice edge. To this end, after introducing basic definitions related to the rheology of viscous fluids in §2a, the assumptions and properties of several variants of the so-called $\mu(I)$ rheology are discussed in §2b, followed by the presentation of the formal definition of stress tensor in granular materials in §2c and details of the already mentioned collisional sea ice rheology (§3). One of the very important aspects of those subjects are effects of polydispersity (i.e. heterogeneity of grain sizes) and methods to account for them in models. Most granular rheologies are formulated for materials with a narrow grain size distribution and their applicability to strongly polydisperse materials remains unexplored. Therefore, insights obtained for sea ice can serve a wider purpose as a test case for granular materials in general. The idealized DEM simulations of simple-shear deformation presented in §4 illustrate some effects not captured by the present sea ice rheology models. In particular, it is shown that the apparent friction coefficient is strongly shear-rate and floe size dependent, and the influence of the largest floes (i.e. the tail of the FSD) on the yield stress, strain–stress relationship and velocity fluctuations is investigated. In §5, conclusions are formulated and possible further directions of research discussed.

2. Selected aspects of rheology of dense granular materials

Anticipating the application of concepts presented in this section to continuum modelling of sea ice, in which the momentum and constitutive equations are formulated in two dimensions

(integrated over ice thickness), the description and formulae in §2a–c below are given for two-dimensional materials as well. Full three-dimensional versions can be found in the cited papers. Cartesian coordinates are used in the horizontal plane, with axes x_i, $i = 1, 2$.

(a) Basic definitions: stress and strain in viscous fluids

Continuum models of granular materials, analogously to models of viscous fluids, are based on the conservation equations for mass and momentum, the general form of which is

$$\frac{\mathrm{D}\rho_b}{\mathrm{D}t} + \rho_b\left(\frac{\partial u_1}{\partial x_1} + \frac{\partial u_2}{\partial x_2}\right) = 0 \quad \text{and} \quad \frac{\mathrm{D}(\rho_b u_i)}{\mathrm{D}t} = \frac{\partial \sigma^c_{i1}}{\partial x_1} + \frac{\partial \sigma^c_{i2}}{\partial x_2} + \rho_b F_i \quad \text{for } i = 1, 2, \tag{2.1}$$

where for any function $f(x_1, x_2, t)$ the material derivative $\mathrm{D}f/\mathrm{D}t = \partial f/\partial t + u_1 \partial f/\partial x_1 + u_2 \partial f/\partial x_2$, t denotes time, u_i denotes the velocity component in the direction x_i, ρ_b is the bulk mass density ($\rho_b = \rho\phi$, with ρ the mass density of the grains and ϕ the solid volume fraction), F_i is the ith component of an external body force (per unit mass), and σ^c_{ij} are components of the Cauchy stress tensor, resulting from external contact forces acting on the surface of the analysed volume (see, e.g., [27]). Apart from equations (2.1), an essential component of continuum models of granular materials are constitutive equations relating stress to deformation rates and bulk material properties. The rate of deformation tensor $\dot{\varepsilon}_{ij}$ is defined in terms of the velocity gradients as

$$\dot{\varepsilon}_{ij} = \frac{1}{2}\left(\frac{\partial u_i}{\partial x_j} + \frac{\partial u_j}{\partial x_i}\right), \tag{2.2}$$

where u_i denotes the velocity component in the direction x_i. For the purpose of the further analysis, it is convenient to introduce the following notation: $\dot{\varepsilon}_i \equiv \dot{\varepsilon}_{ii} = \partial u_i/\partial x_i$ for $i = 1, 2$, and $\dot{\gamma} \equiv \dot{\varepsilon}_{12} = \dot{\varepsilon}_{21} = \frac{1}{2}(\partial u_1/\partial x_2 + \partial u_2/\partial x_1)$. Thus, $\dot{\varepsilon}_i$ and $\dot{\gamma}$ represent the longitudinal and shear strain rates, respectively. The volumetric strain rate is $\dot{\varepsilon}_V = \dot{\varepsilon}_1 + \dot{\varepsilon}_2$, and the pure-shear strain rate $\dot{\varepsilon}_{\mathrm{PS}} = \dot{\varepsilon}_1 - \dot{\varepsilon}_2$. The Cauchy stress tensor σ^c_{ij} is split into two parts, the isotropic pressure p^c and the deviatoric stress $\hat{\sigma}^c_{ij}$

$$\sigma^c_{ij} = -p^c \delta_{ij} + \hat{\sigma}^c_{ij}, \tag{2.3}$$

where δ_{ij} denotes the Kronecker delta and $\hat{\sigma}^c_{11} + \hat{\sigma}^c_{22} = 0$. Analogously to $\dot{\varepsilon}_i$ and $\dot{\gamma}$, the normal and tangential stress components are denoted with $\hat{\sigma}^c_i \equiv \hat{\sigma}^c_{ii}$ (for $i = 1, 2$) and $\tau^c \equiv \hat{\sigma}^c_{12} = \hat{\sigma}^c_{21}$, respectively. The friction coefficient is $\mu = \tau^c/p^c$. For compressible viscous fluids [27]

$$\hat{\sigma}^c_i = 2\eta\dot{\varepsilon}_i + (\zeta - \eta)\dot{\varepsilon}_V \quad \text{and} \quad \tau^c = 2\eta\dot{\gamma}, \tag{2.4}$$

where η is the shear (or dynamic) viscosity and ζ is the bulk viscosity, representing the resistance of a fluid towards rapid changes of volume. In Newtonian, i.e. linearly viscous fluids, η is a scalar. In non-Newtonian fluids, η represents the apparent viscosity and is a function of $\dot{\gamma}$, material properties and, in time-dependent rheologies, time. Time-independent fluids can be broadly divided into purely viscous fluids, for which $\tau^c(\dot{\gamma} = 0) = 0$, and viscoplastic fluids, exhibiting a yield shear stress, i.e. $\tau^c(\dot{\gamma} = 0) > 0$. Notably, the Hibler's viscous-plastic sea ice rheology [20,28] and the collisional rheology described further in §3 both have the general form of (2.3) and (2.4).

(b) $\mu(I)$ rheology

Based on a dimensional analysis of the governing equations describing a simple-shear flow ($\dot{\varepsilon}_{\mathrm{PS}} = \dot{\varepsilon}_V = 0$) of dry granular materials, it has been shown that the friction coefficient μ and the solid volume fraction ϕ are functions of a single, non-dimensional parameter I called the inertial number (e.g. [29])

$$I = \sqrt{\frac{\rho}{p^c}}\dot{\gamma}\bar{d}, \tag{2.5}$$

where $\bar{d}$ is a measure of the average grain diameter (discussed below). Thus, $\mu = \mu(I)$ and $\phi = \phi(I)$ [29–32]. The form of these functions depends on the material properties and, when this rheology

model is extended to more complex types of flows, the flow geometry. In three dimensions, σ_{ij}^c is given by (2.3) with $\hat{\sigma}_{ij}^c$ [30]

$$\hat{\sigma}_{ij}^c = \mu(I) p^c \frac{\dot{\varepsilon}_{ij}}{|\dot{\varepsilon}|}, \tag{2.6}$$

where $|\dot{\varepsilon}|$ is the second invariant of $\dot{\varepsilon}_{ij}$. Hence, the apparent viscosity η depends on both shear rate and pressure. In general, suitable candidates for $\mu(I)$, $\phi(I)$ should reflect the two closely related characteristic properties of dense granular flows: shear-thickening and dilatancy. In other words, they should reflect an increase of the apparent viscosity and volume with increasing shear rates, as the flow evolves from the quasi-static through the dense to the kinetic regime. Widely used phenomenological formulae for $\mu(I)$ and $\phi(I)$ are (e.g. [31])

$$\mu(I) = \mu_0 + \frac{(\mu_\infty - \mu_0)}{(I_0/I + 1)} \quad \text{and} \quad \phi(I) = \phi_0 - c_\phi I, \tag{2.7}$$

where μ_0, μ_∞, I_0, ϕ_0, c_ϕ are adjustable coefficients. Thus, ϕ decreases linearly with I from its maximum value ϕ_0, and μ varies between μ_0 in the quasi-static regime ($I \to 0$) and μ_∞ in the kinetic regime ($I \to \infty$). Both μ_0 and μ_∞ are finite, the behaviour is viscoelastic, i.e. $\tau(\dot{\gamma} = 0) = \mu_0 p^c$. In spite of several limitations (non-locality, long-range correlations, hysteresis effects, etc. typical of granular materials, are not taken into account), as well as problems with applicability of that model to highly inhomogeneous and/or non-stationary flows, and with ill-posedness under some strain combinations [33], the $\mu(I)$ rheology has been found in several studies to satisfactorily represent observational and model data (e.g. [31,34,35]) over a wide range of confining pressures, inertial numbers and materials used, although the spread of values of the fitted coefficients obtained in those studies tends to be rather large and the form of $\mu(I)$ is in some materials more complex than in (2.7), see, e.g., [36,37] for cohesive media. Overall, the $\mu(I)$ rheology performs particularly well for dense flows at low inertial numbers.

From the point of view of the potential application of a $\mu(I)$-type rheology to sea ice (and to highly polydisperse materials in general), an important aspect of the definition of I is its dependence on $\bar{d}$. In the theoretical, numerical and observational studies that led to the formulation of the $\mu(I)$ rheology, narrow grain size distributions were considered, with the average grain diameter used for $\bar{d}$, and little attention was paid to the possible effects of polydispersity. More recently, e.g. in studies on rheology of bidisperse mixtures, $\bar{d}$ is usually computed as a volume-fraction-weighted average grain diameter, although little is known about the suitability of the $\mu(I)$ rheology and the meaning of $\bar{d}$ in materials with very strong polydispersity (see, e.g. discussion in [38]).

It is also worth noting that if $\phi(I)$ is invertible, as in (2.7), I can be computed from ϕ so that, combined with (2.5), the pressure p^c is given as $p^c = p^c(\phi, \dot{\gamma})$, i.e. it depends on both the volume fraction and strain rate (as long as ϕ is sufficiently far from ϕ_0 and $\dot{\gamma} \neq 0$). The relationship $p^c(\phi, \dot{\gamma})$, together with (2.6), makes the rheology applicable in continuum models, where p^c and $\hat{\sigma}_{ij}^c$ have to be computed from available grid-scale variables.

Finally, the inertial number squared, $I^2 = \rho \dot{\gamma}^2 \bar{d}^2 / p^c$, is a ratio of the bulk measure of the inertial pressure to the confining pressure in the material. Based on the additive property of stress, it has been shown recently that the $\mu(I)$ rheology can be extended to a wide range of cohesive materials and suspensions (i.e. submerged flows), provided that I is computed in a more general way, i.e. as a ratio of the linear combination of all stresses related to the grains' motion to the linear combination of stresses related to grain contacts [39,40]. Thus—again, importantly for potential applications to sea ice—cohesive and viscous interactions associated with the presence of fluid in spaces between grains can be included together with the 'standard' elastic and frictional grain–grain interactions.

(c) Definition of stress tensor in granular materials

DEM methods are an invaluable source of information on granular flows as they allow to relate processes acting at different scales, from grain-level interactions, through contact/force chains

and grain clusters, to bulk material properties relevant for continuum models. Obtaining that multi-scale information from observational data is an unattainable goal. Obviously, in order for DEM results to be useful, the relevant bulk variables must be computed from information available at the grain level in a proper way. Considering the wide popularity of DEM methods, it might seem surprising that misconceptions regarding the computation of volume-averaged stress are quite common, and several papers are devoted to alternative definitions of that quantity and their interpretation. It is therefore useful to provide here a summary of that computation and the relevant concepts.

In the momentum equations (2.1), there are two terms that are directly related to processes acting at the grain level. One is the divergence of the Cauchy strain tensor on the right-hand side of (2.1): as forces in granular materials are transmitted through grain–grain interactions, the stress applied to the surface of a given volume of that material can be expressed as a sum of grain–grain stresses within that volume, so that, for an assembly of grains occupying a given volume V the Cauchy (or contact) stress is (e.g. [41,42])

$$\sigma_{ij}^{c} = \frac{1}{V}\sum_{n=1}^{N_c} f_{n,i}^{c} l_{n,j}^{c}, \tag{2.8}$$

where N_c is the total number of contacts (within V, as well as contacts with 'outside' grains through the boundary of V; see figure 1*a*), $f_{n,i}^{c}$ denotes the ith component of the contact force at the nth contact, and $l_{n,j}^{c}$ is the jth component of the vector connecting the centres of mass of grains participating in that contact. The second of the two terms mentioned above is the advective term in the material derivative on the left-hand side of (2.1), which after some rearrangements can be expressed as $\rho_b(\partial(u_i u_1)/\partial x_1 + \partial(u_i u_2)/\partial x_2)$. In many applications, it is useful to split the instantaneous velocity u_i into its mean $\bar{u}_i$ and fluctuating part u_i', related to the motion of individual grains: $u_i = \bar{u}_i + u_i'$. By definition, $\overline{u_i'} = 0$, so that the advective term becomes $\rho_b(\partial \overline{u_i}\,\overline{u_1}/\partial x_1 + \partial \overline{u_i}\,\overline{u_2}/\partial x_2) + \rho_b(\partial \overline{u_i' u_1'}/\partial x_1 + \partial \overline{u_i' u_2'}/\partial x_2)$. In a continuum model, the first part of this sum can be directly computed from variables resolved at the grid-level. The second part, analogous to the Reynolds stress in models of turbulent flows, describes the momentum flux due to 'random', sub-grid-scale grain motion. As it has an analogous form to the Cauchy stress term, they can be combined into one tensor $\sigma_{ij}^{t} = \sigma_{ij}^{c} + \sigma_{ij}^{k}$, where $\sigma_{ij}^{k} = \rho\phi\overline{u_i' u_j'}$ is the momentum flux (or kinetic stress) tensor. For finite-size grains, $\overline{u_i' u_j'}$ contains contributions from the linear and angular velocities of the grains (see [43] and [41] for detailed derivation), so that

$$\sigma_{ij}^{k} = -\frac{1}{V}\sum_{n=1}^{N_g} m_n u_{n,i}' u_{n,j}' + \frac{1}{2V}\sum_{n=1}^{N_g} M_n \Omega_n^2 \delta_{ij}, \tag{2.9}$$

where N_g is the number of grains, m_n and M_n denote the mass and moment of inertia of the nth grain, respectively (for a disc $M_n = \frac{1}{2} m_n r_n^2$, where r_n is the disc's radius), and $\Omega_n = |\boldsymbol{\Omega}_n|$. The rotational component of σ_{ij}^{k}, equal to the average spin kinetic energy, can be interpreted as a tensile stress related to the centrifugal effects of grains' rotation (note that this term is always positive, i.e. it has the opposite sign to the contact pressure; its contribution to the shear stress is zero).

Both (2.8) and (2.9) can be directly computed from the results of DEM models and belong to the standard output of most available DEM codes. The already mentioned controversies are related not to the computation of σ_{ij}^{c}, σ_{ij}^{k} and σ_{ij}^{t}, but rather to their usage and interpretation. In particular, the first part of the kinetic stress in (2.9) is present only if stress is formulated in the Eulerian frame of reference and vanishes if a Lagrangian approach is used (compare the derivation and conclusions in [41,43]). Similarly, σ_{ij}^{c} alone should be used when the quantity of interest is the stress exerted by a granular material on walls and other structures, but both σ_{ij}^{c} and σ_{ij}^{k} should be parametrized in continuum models based on slowly varying variables. As far as σ_{ij}^{k} is concerned, computation of $\bar{u}_i$ and u_i' is non-trivial if the flow is very complex, non-stationary and, especially, if the sizes of grains are not very small compared with the size of the domain (as will be the case in

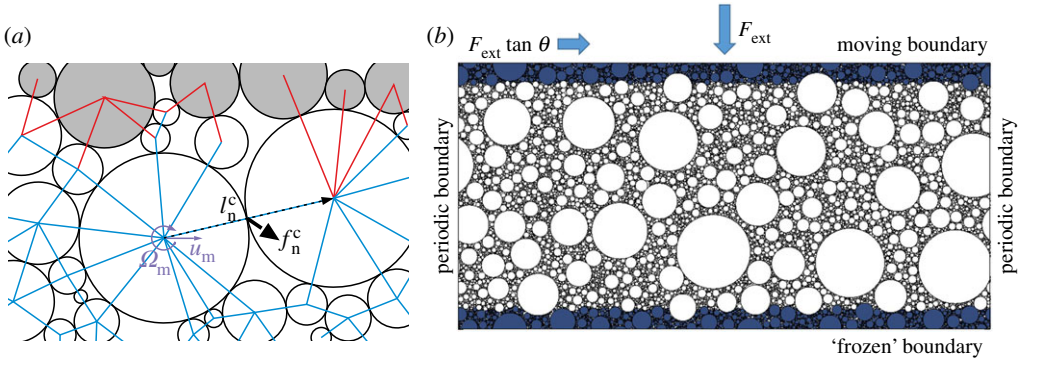

Figure 1. Stress in a sheared granular material. (*a*) the averaged stress as a sum of two components: contact forces between grains within the control volume *V* (blue lines, white circles) and with boundary grains (red lines, grey circles); and kinetic energy of grains in *V* (violet arrows). (*b*) a standard DEM set-up for studying strain–stress relationships under simple-shear deformation (see §4a). (Online version in colour.)

simulations described in §4). Therefore, in some studies σ_{ij}^k is computed from the total velocities u_i instead of u_i'. This amounts to including the whole advective term in the stress-divergence term on the right-hand side of (2.1); accordingly, it should be removed from the left-hand side. Moreover, although, as is often noted (e.g. [43]), any non-divergent component can be added to σ_{ij}^k without any influence on stress divergence occurring in the momentum equation, that operation obviously has a substantial influence on the stress itself. In particular, it makes any inferences on the relative contribution of kinetic and contact stresses to the total stress meaningless. While in many cases $\sigma_{ij}^k \ll \sigma_{ij}^c$ when σ_{ij}^k is computed based on velocity anomalies, it is not true when the mean advection is included in the momentum-flux tensor. In general, even if u_i' are used, the ratio $\sigma_{ij}^k/\sigma_{ij}^c$ is very sensitive to the computation of $\bar{u}_i$ and u_i'. From the point of view of the momentum balance, the divergence of σ_{ij}^c and σ_{ij}^k can be compared, not the stresses themselves. Similar caution should be taken when computing the friction coefficient μ. It was defined in §2a as $\mu = \tau^c/p^c$. An analogous version $\mu^t = (\tau^c + \tau^k)/(p^c + p^k)$ suffers from the problems described above and its usefulness is therefore rather limited.

3. Collisional rheology for sea ice

The collisional rheology has been formulated in the 1980s in a series of papers by Shen and colleagues [17,18,44] and subsequently extended by [45,46] and others. The original model was formulated for sea ice with ice concentration A, composed of identical disc-shaped floes with diameters d, thickness h, mass density ρ and restitution coefficient ϵ, and subject to deformation described by a strain rate tensor $\dot{\varepsilon}_{ij}$, defined in (2.2). Based on equations describing the momentum transfer and energy dissipation during inelastic floe–floe collisions, with several assumptions regarding the geometry of the problem (see further), [18] obtained the formula for the collisional stress tensor σ_{ij}^C in the form (2.3) and (2.4), with p, η and ζ given by

$$p = \frac{\psi}{2^{1/2}\pi}\left(\frac{v'}{\bar{d}}\right)^2, \quad \eta = \frac{\psi}{3}\frac{v'}{\bar{d}}, \quad \zeta = 3\eta, \quad \text{with } \psi = \frac{\rho\bar{d}^2 h(1+\epsilon)}{4\pi} f(A), \tag{3.1}$$

where $f(A)$ is a function of the actual and maximum possible ice concentration A_0 (equal to 0.91 for equal-size discs), $f(A) = A^{3/2}/(A_0^{1/2} - A^{1/2})$, v' denotes the ensemble average magnitude of the fluctuation velocity of the discs, and $\bar{d} = d$ (for a more general formulation valid for polydisperse sea ice with relatively narrow FSDs, see [45]). A fundamental assumption underlying the above model is that sea ice behaves as a granular gas in which 'cooling' due to inelastic collisions is balanced by 'heating' by shear, and the floes do not change their velocities between collisions.

Additional assumptions are, first, a predetermined form of the directional distribution function of floes' fluctuations, and second, large magnitude of those fluctuations compared with the mean shear rate, or to differences between the mean velocities of interacting floes: $v' \gg \dot{\gamma}\bar{d}$. This allows to parametrize the ratio $v'/\bar{d}$ in (3.1) as a function of ϵ and $\dot{\varepsilon}_{ij}$. However, although this condition is typically fulfilled in the MIZ [18,45], the model suffers from limitations that are intrinsic features of granular gases, including the inelastic collapse, i.e. infinitely high collision rates as $A \to A_0$ (although, at the same time, high compactness is required for the estimation of collision rates to be valid). A related problem is the assumption of the uniform distribution of floes on the sea surface, which is realistic only if ϵ is sufficiently high to prevent clustering instability (e.g. [47]). Whereas high ϵ values were used in [18,19], more recent field and laboratory studies suggest that collisions in real sea ice are close to inelastic ([48,49] and references there).

A substantial development of the collisional rheology was relaxing the simple-shear assumption of [18]. Based on suggestions formulated in the original paper [18] and research on flows of dense granular materials [50,51], Feltham [19] developed a sea ice model for the MIZ with a combined plastic (Hibler's) and collisional rheology in which the simplified estimation of v' was replaced with a full evolution equation for the granular temperature $T \equiv v'^2/2$. The equation includes advection and diffusion terms, as well as source functions describing the input of T due to the work done by the forces from the ocean and atmosphere, and dissipation due to floe–floe interactions (see [19] for details and derivation). However, the computation of those source terms requires several assumptions, some of which are grounded in research on dry granular materials that is not necessarily directly transferable to sea ice, and others, rather debatable.

4. Role of floe size distributions in shear deformation in marginal ice zone

(a) Model set-up

As mentioned in the introduction, a DEM model is used in this study to illustrate selected aspects of the discussed processes. To this end, the DESIgn model [52] is run in an idealized configuration suitable for an analysis of simple-shear scenarios, routinely used for studying rheological properties of granular materials ([29,36,37,39,53,54] and many more). For each group of model runs, a set of N_g disc-shaped grains (ice floes) with the tapered power law FSD $p(r)$ is generated with the transformation method described in [55]

$$p(r) \sim r^{-\alpha} \exp\left(\frac{-r}{\beta}\right), \tag{4.1}$$

where the exponent α and the scale parameter β are both positive. The total surface area S_{tot} of each floe set is constant, $S_{\mathrm{tot}} = 1500^2\,\mathrm{m}^2$, but the sets differ in terms of α and β (and thus the value of N_g). Hence, they can be interpreted as the same area of ice broken into floes of different sizes. For the combinations of α and β considered (1.0, 1.2, …, 2.0 and 20, 30, 50, 75, 100, 150, 200 m, respectively), the minimum floe diameter d_{min} remains fairly constant at approximately 2 m, but the maximum diameter d_{max} varies roughly linearly with β (and independently of α) from approximately 220 m for $\beta = 20$ m to ~870 m for $\beta = 200$ m. Hence, the surface area of the largest floe varies from ~1.5% to over 26% of S_{tot}. For all sets, the so-called size span $s = (1 - d_{\mathrm{min}}/d_{\mathrm{max}})/(1 + d_{\mathrm{min}}/d_{\mathrm{max}})$, often used as a measure of polydispersity of granular materials, exceeds 0.98, and is thus larger than in most studies where the influence of s on the bulk material properties is analysed (see [56,57] and references there). The surface-area-weighted floe diameter $\bar{d}_a$ is

$$\bar{d}_a = \frac{2\int_0^\infty r^3 p(r)\,\mathrm{d}r}{\int_0^\infty r^2 p(r)\,\mathrm{d}r} = 2\beta(3-\alpha). \tag{4.2}$$

All floes have the mass density $\rho = 920\,\mathrm{kg\,m^{-3}}$, thickness $h = 0.5$ m, elastic modulus $E = 5 \times 10^9$ Pa, Poisson's ratio $\nu = 0.33$ and friction coefficient $\mu_g = 0.7$. All details of the contact model and its numerical implementation can be found in electronic supplementary material of [52].

During the preparation phase of each run group, the floes are placed randomly, without overlaps, within a square domain with surface area $S_{\mathrm{tot}}/0.85$, which is then uniformly compressed to a smaller area $S_{\mathrm{tot}}/0.90$ (so that the domain dimensions are $L_{x_1} = L_{x_2} = 1581$ m) and left to relax over a period of time sufficient for the stresses and velocities to decrease to insignificantly small values. Subsequently, the domain is divided into three regions (figure 1*b*): the lower, 'frozen' boundary for $x_2 < 0.1L_{x_2}$, where the velocities of all floes are set to zero; the upper boundary for $x_2 > 0.9L_{x_2}$, where the floes move collectively as one rigid body subject to an external force $-F_{\mathrm{ext}}$ in the x_2-direction and $F_{\mathrm{ext}} \tan\theta$ in the x_1-direction; and the middle region, where the full linear and angular momentum equations are solved for each floe (see [52]). The boundaries in the x_1-direction are periodic, L_{x_1} is kept constant at the value given above, and L_{x_2} varies accordingly to the applied confining pressure. Three values of F_{ext} are considered, producing the average pressure in the material $p_1 \sim 60$ kPa, $p_2 \sim 6$ kPa and $p_3 \sim 0.6$ kPa, respectively (which corresponds to the internal ice pressure resulting from a moderate on-ice wind stress of 0.3 Pa acting over the distance of 100 km, 10 km and 1 km; thus p_1 represents pressure conditions in the inner MIZ, and p_3 conditions close to the ice edge). For each set of ice floes and each F_{ext}, θ is increased from 0 to 24° with steps of 1.5°, and the evolution of the global and per-floe variables of interest is recorded for further analysis, described in §4b. In particular, with $\bar{d} = \bar{d}_a$ given by (4.2) and the domain-averaged shear rate $\dot{\gamma} = V_{\mathrm{top}}/L_{x_2}$, where V_{top} is the simulated, time averaged x_1-velocity of the upper boundary, the inertial number (2.5) becomes

$$I = \frac{2\beta(3-\alpha)V_{\mathrm{top}}}{L_{x_2}} \sqrt{\frac{\rho}{p^c}}. \tag{4.3}$$

The contact pressure p^c, shear stress τ^c and friction coefficient μ are computed from σ_{ij}^c defined in (2.8). Notably, under stationary conditions in the simple-shear scenario, the momentum equation (2.1) reduces to the balance between the divergence of the contact and kinetic stresses (with, possibly, the external body force added). Therefore, the analysis in §4b below concentrates on the contact stresses, with references to the velocity anomalies and momentum flux when it adds to the understanding of the underlying dynamics.

All simulations are repeated in two versions: with boundary forcing only (version A); and with ice–water drag, assuming ocean at rest (version B). In version B, the ith component of the drag force on a floe with radius r is $F_{w,i} = -\pi r^2 \rho_w C_{d,w} |u| u_i$, $\rho_w = 1027\,\mathrm{kg\,m^{-3}}$ is water density, $C_{d,w} = 5 \times 10^{-3}$ is water–ice drag coefficient and $|u|$ is the floe's speed.

(b) Results

The model version A, without any forces from the ocean or atmosphere, represents a dry granular material (and is thus analogous to the treatment of sea ice in the collisional rheology). The results of that version are very useful as a reference case, for which the role of polydispersity in the material's response to shear deformation can be analysed in detail. Figure 2*a* shows the shear stress τ^c in function of $\dot{\gamma}$ and β for the three confining pressure values considered. Roughly, three regions of $(\dot{\gamma}, \tau^c)$ can be distinguished in each group of curves: the quasi-static regime, where $\dot{\gamma}$ is very small and the motion of the upper boundary results from local rearrangements of groups of grains rather than from the net deformation of the sample, so that the variance of V_{top} exceeds its mean value (black crosses in figure 2*a*; notably, some rearrangements are present even at $\theta = 0$, i.e. when no macroscopic deformation is occurring); the dense flow regime, where τ^c increases smoothly with $\dot{\gamma}$ and with β; and the rapid flow regime, in which τ^c saturates towards an approximately constant, floe size- and shear rate-independent value. Characteristically, the range of $\dot{\gamma}$ separating the quasi-static from the rapid flow regime decreases with decreasing confining pressure, and the value of θ for which the material begins to flow increases with increasing β. In other words, the wider the FSD and the higher the $\bar{d}$, the higher the shear pressure the material can sustain without undergoing macroscopic deformation other than very slow creep accommodated by local groups of floes. At intermediate shear rates, for a given value of $\dot{\gamma}$ the shear pressure τ^c differs by a factor of two or more between $\beta = 20$ m and $\beta = 200$ m, and vice versa, a given shear

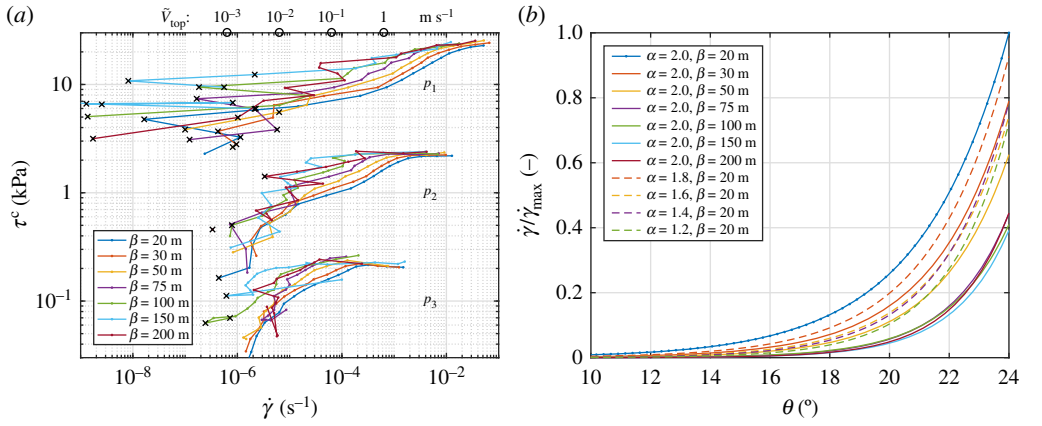

Figure 2. Influence of FSDs on the model response to shear deformation: shear stress τ^c versus shear rate $\dot{\gamma}$ for $\alpha = 2.0$ and the three values of pressure considered (*a*); and the dependence of $\dot{\gamma}$ on FSD properties for selected combinations of α and β (*b*). In (*a*), black crosses mark data points for which variance of V_{top} exceeds its mean value. For orientation, circles at the upper boundary show approximate values of V_{top} (computed from average L_{x_2} over all runs) corresponding to $\dot{\gamma}$ at the bottom axis. In (*b*), all values are scaled with $\dot{\gamma}_{max}$, the largest strain rate among all cases considered (for $\alpha = 2.0$, $\beta = 20$ m and $\theta = 24^\circ$). (Online version in colour.)

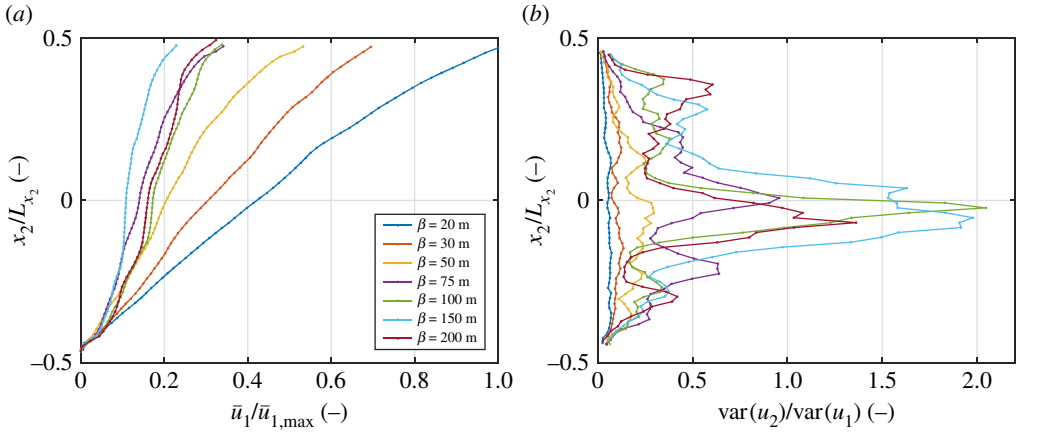

Figure 3. Average velocity profiles $\bar{u}_1(x_2/L_{x_2})$ (*a*) and ratio of variances of the two velocity components var(u_2)/var(u_1) (*b*) for different values of β (colours). In (*a*), all values are scaled with $\bar{u}_{1,max}$, the largest velocity among all cases plotted. Results for $\alpha = 2.0, \theta = 24^\circ$. (Online version in colour.)

stress leads to much slower deformation of ice when the floes are large than when they are small (figure 2*b*).

Those FSD-related effects, including the decrease of $\dot{\gamma}$ with increasing β and/or decreasing α (figure 2*b*), are closely related to the presence of the largest floes in the ensemble. If all floes are small, $d \ll L_{x_2}$, deformation is uniform over the entire domain, the velocity profiles $u_1(x_2)$ are approximately linear and the velocity fluctuations in the x_2-direction are small compared with those in the x_1 direction (figure 3*a*,*b*). The presence of floes with diameters comparable with the size of the domain disrupts the uniform character of the flow. As the floes move as rigid bodies, velocity u_1 in their direct surroundings is x_2-independent, so that the actual shear deformation has to be accommodated in one or several relatively narrow bands (see the velocity profile for $\beta = 200$ m in figure 3*a*)—the net flow becomes sensitive not only to the sizes, but

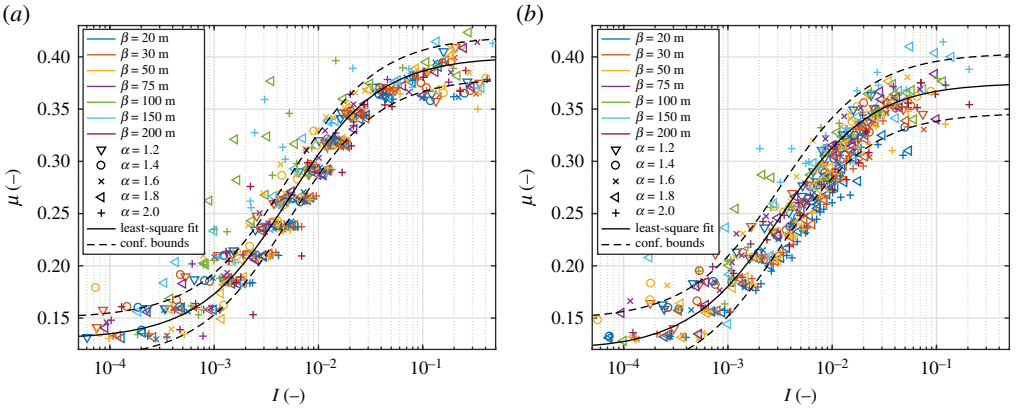

Figure 4. $\mu(I)$ for different combinations of α (symbols), β (colours), θ and p in simulations from version A (*a*) and B (*b*). The black curves show the least-square fit of equation (2.7), dashed curves mark the 95% confidence interval. (Online version in colour.)

also to the relative positions of the small number of the largest floes and, moreover, it has a fully two-dimensional character, i.e. due to small floes flowing around the edges of the large ones, the variance of u_2 becomes comparable or even larger than the variance of u_1 (curves for $\beta \geq 75$ m in figure 3*b*). The net, macroscopic result is a larger stiffness of the ice described above, i.e. lower strain rates for a given shear stress or, *vice versa*, higher stress under a given strain rate. Importantly as well, large size span of floes leads to strong temporal fluctuations of stress, related to phases of a relatively smooth flow separated by events of sudden blocking (not shown).

In spite of the very wide range of I and τ^c obtained for the combinations of FSD properties (α, β) and forcing (F_{ext}, θ) considered (figure 2*a*), the resulting combinations of μ and I all fall onto a relatively well-defined curve (figure 4*a*) which can be well approximated with formula (2.7). Although the fit is not perfect, the majority of the data points lie within the 95% confidence interval. The fitted coefficients for version A are: $\mu_0 = 0.13$, $\mu_\infty = 0.40$ and $I_0 = 6.8 \times 10^{-3}$. Thus, the area-weighted mean floe diameter $\bar{d}_a$, used in the computation of I, seems a suitable measure of the average floe size. Essentially, all data points in figure 4*a* that strongly deviate from the $\mu(I)$ curve correspond to $\beta \geq 100$ m, i.e.situations with the already mentioned localized, transient jamming events that affect the average values of stress and strain, and illustrate the deficiency of the $\mu(I)$ rheology in capturing the material behaviour during abrupt changes of strain rates. Overall, however, μ varies smoothly with I and, as will be discussed further in §5, increases from very low values in the quasi-static regime towards much higher values in the inertial regime. The situation does not change substantially when the ice–ocean drag is added (figure 4*b*), although, as expected, the range of obtained shear rates and thus inertial numbers is narrower (the unrealistically high $\dot{\gamma}$ values in version A, figure 2*a*, are removed). A less trivial result is that transient jamming at high $\bar{d}_a$ is less frequent in version B than in version A (a smaller number of 'outliers' in figure 4*b* than in figure 4*a*).

Finally, in both versions and in all cases considered the ice concentration A (equivalent to the volume fraction ϕ) decreases with increasing I, but, unlike assumed in (2.7), the relationship is not linear and is FSD dependent (figure 5). As the insets in figure 5 show, $\phi = \phi_0 - c_1 \tanh(c_2 I^{1/2})$ gives a good fit to the data, provided ϕ_0, c_1, c_2 are not constant, but functions of α and β. Clearly, although the sensitivity of ϕ to FSD properties is not surprising, this property is disadvantageous in practical applications. On the other hand, however, considering the overall small range of variability of ϕ over a wide range of confining pressures and shear rates, using a single, linear formula (2.7) should be acceptable in practice.

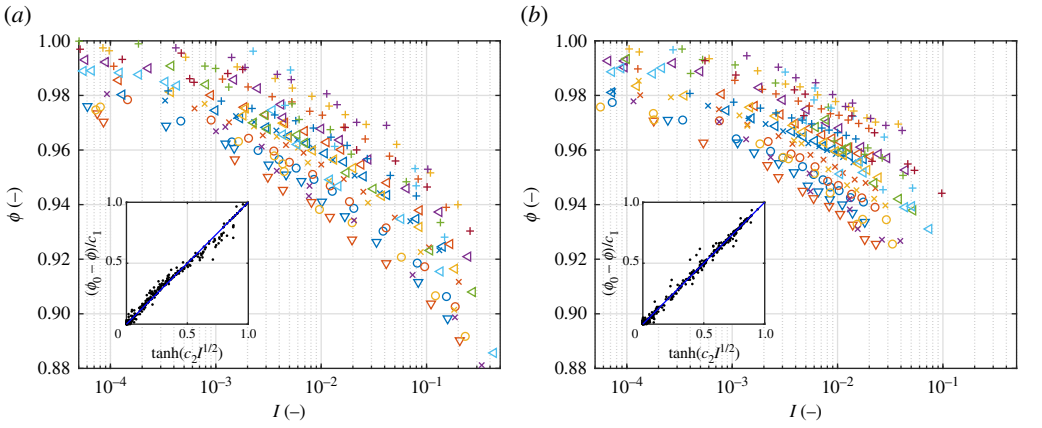

Figure 5. $\phi(I)$ for different combinations of α, β, θ and p (for legend, see figure 4) in simulations from version A (*a*) and B (*b*). The insets show the least-square fit to the data of function $\phi = \phi_0 - c_1 \tanh(c_2 I^{1/2})$, with ϕ_0, c_1, c_2 FSD dependent (see text for details). (Online version in colour.)

5. Discussion and conclusion

Granular materials are mesoscopic—in their dynamics, the microscopic (grain-level) temporal and spatial scales are not well separated from the macroscopic scales. The lack of scale separation is related not only to the fairly large ratio of grain size to the dimensions of systems typically analysed in practical problems (or, equivalently, relatively small number of grains within an analysed volume), but, most importantly, to the nature of interactions between grains [47,58,59]. Thus, mesoscopy is a generic feature of those materials, manifesting itself in phenomena unique to them: a tendency to form clusters of grains, non-local character of macroscopic properties, history effects, scale dependence of stress, long-length correlations associated with force networks, arches of grains, etc. It is not surprising that those effects are amplified in strongly polydisperse materials, in which a wide size span of grains additionally blurs the boundary between micro- and macro-scales: when the grain-size distributions are heavy-tailed, contact and force networks tend to be fractal (see, e.g., [8,54,56,57], and references there). Another feature, closely related to the fractal, 'openwork' character of force networks, is the fact that the forces are carried primarily by a small subset of the largest grains. Those grains build a skeleton of the force network and stay in a semi-permanent contact with each other, while smaller grains in regions not participating in force transmission constantly rearrange their positions and take part in relatively short-lived collisions (as analysed in detail in [8]). Therefore, there is no clear boundary between the 'collisional regime' and 'permanent-contact regime'. To the contrary, different types of contacts coexist and the range of applicability of collisional-type rheologies is hard to define.

Not surprisingly, all those properties lead to difficulties in continuum modelling, for which separation of scales is a prerequisite. Yet another difficulty—contrary to those mentioned above related specifically to sea ice—are increasing spatial resolutions of continuum sea ice models, especially those operated at regional and local scales. Although, indisputably, that development is very positive, the drawback is that even in the MIZ, where ice floes are relatively small, continuum rheologies have to deal with floe sizes comparable with mesh sizes of the models. The results presented in this paper suggest that, on the one hand, the average stress can be reliably computed and the strain–stress relationships remain relatively stable up to high floe diameter to mesh size ratios, but, on the other hand, the information on FSD properties is crucial for that computation.

Another information that might play a role, not analysed in this study (and hardly taken into account in sea ice research in general) are floe shapes. In the simulations in §4, the floes were disc-shaped and no rolling resistance was included in the contact model. This might explain the

rather low values of friction coefficients obtained (note that no attempt was made to calibrate the model to any real MIZ scenario; a sensitivity analysis to model parameters will be performed in a subsequent study). The sparse evidence available, based on recent ice tank experiments and DEM simulations, indicates that floe shapes influence the stability of force networks and therefore stress in the ice, as well as ice-induced loads on structures (e.g. [60]). At the same time, whereas studies on granular materials with multi-shaped grains generally confirm the sensitivity of force networks and bulk properties to grain shape, they also suggest that shape becomes less important in materials with wide grain size spans (e.g. [61,62]). Applied to sea ice, this indicates that floe shapes might be less important for rheology of ice with wide FSDs—like that analysed in this paper—than that of ice with narrow FSDs, e.g. in ice freshly broken by waves (see [63] for an example).

Apart from the influence of FSDs on stress in the ice, a very robust feature clearly seen in the results presented in this paper (and, again, typical for granular materials) is the dependence of the friction coefficient μ on the shear rate $\dot{\gamma}$. In the Hibler's sea ice rheology, $\mu = 2\dot{\gamma}/(e^2\Delta)$, where $\Delta^2 = \dot{\varepsilon}_V^2 + e^{-2}(\dot{\varepsilon}_{PS}^2 + 4\dot{\gamma}^2)$ and e denotes eccentricity of the elliptical yield curve [20,28]. Thus, in a simple-shear flow $\mu = e^{-1}$ is a constant (equal to 0.5 when a typical value $e = 2$ is used). It is easy to show that in the collisional rheology described in §3 μ is $\dot{\gamma}$-independent as well. In the original formulation [18], $\mu = 4\pi/3(v'/\bar{d})^{-1}\dot{\gamma}$, and under simple-shear deformation $v'/\bar{d} \sim \dot{\gamma}$, which makes μ depend only on the restitution coefficient. In the version of Feltham [19] $v' = \sqrt{2T}$ and the granular temperature T is computed from the full turbulent-energy conservation equation. However, when applied to a simple-shear scenario, this model predicts a constant μ as well. Thus, both the Hibler's and the collisional rheologies disregard the increase of the friction coefficient with shear rate and floe size. Because, as said, this effect is very pronounced in sheared granular flows, a rheology model suitable for the MIZ—as well as for regions in straits, channels or near the coasts, where sheared motion of strongly fragmented ice takes place—should take it into account. In spite of its limitations and deficiencies, a $\mu(I)$-type rheology analysed in this paper seems a good starting point for developing such a rheology model.

Data accessibility. The code of the DESIgn model is freely available on the Internet, see [52]. Input files and configuration scripts necessary to reproduce the results from this paper can be obtained from the author.

Conflict of interest declaration. I declare I have no competing interests.

Funding. This work has been financed by Polish National Science Centre project no. 2018/31/B/ST10/00195 (Observations and modelling of sea ice interactions with the atmospheric and oceanic boundary layers).

Acknowledgements. All calculations were carried out at the Academic Computer Centre (TASK) in Gdańsk, Poland. I am very grateful to Hayley Shen for her very insightful comments on the initial version of this paper.

References

1. Horvat C. 2022 Floes, the marginal ice zone and coupled wave-sea-ice feedbacks. *Phil. Trans. R. Soc. A* **380**, 20210252. (doi:10.1098/rsta.2021.0252)
2. Montiel F, Mokus N. 2022 Theoretical framework for the emergent floe size distribution in the marginal ice zone: the case for log-normality. *Phil. Trans. R. Soc. A* **380**, 20210257. (doi:10.1098/rsta.2021.0257)
3. Dumont D. 2022 Marginal ice zone dynamics: history, definitions and research perspectives. *Phil. Trans. R. Soc. A* **380**, 20210253. (doi:10.1098/rsta.2021.0253)
4. Horvat C, Tziperman E, Campin J. 2016 Interaction of sea ice floe size, ocean eddies, and sea ice melting. *Geophys. Res. Lett.* **43**, 8083–8090. (doi:10.1002/2016GL069742)
5. Herman A. 2011 Molecular-dynamics simulation of clustering processes in sea-ice floes. *Phys. Rev. E* **84**, 056104. (doi:10.1103/PhysRevE.84.056104)
6. Rabatel M, Labbé S, Weiss J. 2015 Dynamics of an assembly of rigid ice floes. *J. Geophys. Res.* **120**, 5887–5909. (doi:10.1002/2015JC010909)
7. Herman A. 2013 Numerical modeling of force and contact networks in fragmented sea ice. *Ann. Glaciol.* **54**, 114–120. (doi:10.3189/2013AoG62A055)

8. Herman A. 2013 Shear-jamming in two-dimensional granular materials with power-law grain-size distribution. *Entropy* **15**, 4802–4821. (doi:10.3390/e15114802)
9. Ardhuin F, Otero M, Merrifield S, Grouazel A, Terrill E. 2020 Ice breakup controls dissipation of wind waves across Southern Ocean sea ice. *Geophys. Res. Lett.* **47**, e2020GL087699. (doi:10.1029/2020GL087699)
10. Herman A. 2021 Spectral wave energy dissipation due to under-ice turbulence. *J. Phys. Oceanogr.* **51**, 1177–1186. (doi:10.1175/JPO-D-20-0171.1)
11. Bateson A, Feltham D, Schröder D, Hosekova L, Ridley J, Aksenov Y. 2020 Impact of floe size distribution on seasonal fragmentation and melt of Arctic sea ice. *Cryosphere* **14**, 403–428. (doi:10.5194/tc-14-403-2020)
12. Boutin G, Williams T, Rampal P, Olason E, Lique C. 2020 Impact of wave-induced sea ice fragmentation on sea ice dynamics in the MIZ. In *Proc. 25th IAHR Int. Symp. on Ice, Trondheim, Norway, 23–25 Nov 2020* (eds KA *et al.*).
13. Li J, Babanin A, Liu Q, Voermans J, Heil P, Tang Y. 2021 Effects of wave-induced sea ice break-up and mixing in a high-resolution coupled ice-ocean model. *J. Mar. Sci. Eng.* **9**, 365. (doi:10.3390/jmse9040365)
14. Rynders S, Aksenov Y, Feltham D, Nurser A, Madec G. 2022 Impact of granular behaviour of fragmented sea ice on marginal ice zone dynamics. In *IUTAM Symp. on Physics and Mechanics of Sea Ice* (eds J Tuhkuri, A Polojärvi), IUTAM Bookseries, vol. 39, pp. 261–274. Switzerland: Springer Nature. (doi:10.1007/978-3-030-80439-8–13)
15. Cooper VT, Roach LA, Thomson J, Brenner SD, Smith MM, Meylan MH, Bitz CM. 2022 Wind waves in sea ice of the western Arctic and a global coupled wave-ice model. *Phil. Trans. R. Soc. A* **380**, 20210258. (doi:10.1098/rsta.2021.0258)
16. Auclair J-P, Dumont D, Lemieux J-F, Ritchie H. 2022 A model study of convergent dynamics in the marginal ice zone. *Phil. Trans. R. Soc. A* **380**, 20210261. (doi:10.1098/rsta.2021.0261)
17. Shen H, Hibler III W, Leppäranta M. 1986 On applying granular flow theory to a deforming broken ice field. *Acta Mech.* **63**, 143–160. (doi:10.1007/BF01182545)
18. Shen H, Hibler III W, Leppäranta M. 1987 The role of floe collisions in sea ice rheology. *J.Geophys. Res.* **92**, 7085–7096. (doi:10.1029/JC092iC07p07085)
19. Feltham D. 2005 Granular flow in the marginal ice zone. *Phys. Trans. R. Soc. A* **363**, 1677–1700. (doi:10.1098/rsta.2005.1601)
20. Hibler III W. 1979 A dynamic–thermodynamic sea ice model. *J. Phys. Oceanogr.* **9**, 817–846. (doi:10.1175/1520-0485(1979)009<0815:ADTSIM>2.0.CO;2)
21. Tremblay LB, Mysak L. 1997 Modeling sea ice as a granular material, including the dilatancy effect. *J. Phys. Oceanogr.* **27**, 2342–2360. (doi:10.1175/1520-0485(1997)027<2342:MSIAAG>2.0.CO;2)
22. Wilchinsky A, Feltham D. 2006 Modelling the rheology of sea ice as a collection of diamond-shaped floes. *J. Non-Newton. Fluid Mech.* **138**, 22–32. (doi:10.1016/j.jnnfm.2006.05.001)
23. Sayed M, Neralla V, Savage S. 1995 Yield conditions of an assembly of discrete ice floes. In *Proc. 5th Int. Offshore Polar Engng Conf., The Hague, The Netherlands, 11–16 June 1995*, vol. II, pp. 330–335. Mountain View, CA: International Society of Offshore Polar Engineers.
24. Gutfraind R, Savage S. 1997 Marginal ice zone rheology: comparison of results from continuum-plastic models and discrete-particle simulation. *J. Geophys. Res.* **120**, 12 647–12 661. (doi:10.1029/97JC00124)
25. Gutfraind R, Savage S. 1997 Smoothed particle hydrodynamics for the simulation of broken-ice fields: Mohr–Coulomb-type rheology and frictional boundary conditions. *J. Comput. Phys.* **134**, 203–215. (doi:10.1006/jcph.1997.5681)
26. Gutfraind R, Savage S. 1998 Flow of fractured ice through wedge-shaped channels: smoothed particle hydrodynamics and discrete-element simulations. *Mech. Mater.* **29**, 1–17. (doi:10.1016/S0167-6636(97)00072-0)
27. Irgens F. 2014 *Rheology and non-Newtonian fluids*, p. 190. Switzerland: Springer Int.
28. Feltham D. 2008 Sea ice rheology. *Annu. Rev. Fluid Mech.* **40**, 91–112. (doi:10.1146/annurev.fluid.40.111406.102151)
29. da Cruz F, Emam S, Prochnow M, Roux JN, Chevoir F. 2005 Rheophysics of dense granular materials: discrete simulation of plane shear flows. *Phys. Rev. E* **72**, 021309. (doi:10.1103/PhysRevE.72.021309)
30. Jop P, Forterre Y, Pouliquen O. 2006 A constitutive law for dense granular flows. *Nature* **441**, 727–730. (doi:10.1038/nature04801)

31. Jop P. 2015 Rheological properties of dense granular flows. *C. R. Phys.* **16**, 62–72. (doi:10.1016/j.crhy.2014.12.001)
32. GDR MD. 2004 Dense granular flows. *Eur. Phys. J. E* **14**, 341–365. (doi:10.1140/epje/i2003-10153-0)
33. Schaeffer D, Barker T, Tsuji D, Gremaud P, Shearer M, Gray J. 2019 Constitutive relations for compressible granular flow in the inertial regime. *J. Fluid Mech.* **874**, 926–951. (doi:10.1017/jfm.2019.476)
34. Forterre Y, Pouliquen O. 2009 Granular flows. *Séminaire Poincaré* **XIII**, 69–100.
35. Gaume J, Chambon G, Naaim M. 2011 Quasistatic to inertial transition in granular materials and the role of fluctuations. *Phys. Rev. E* **84**, 0513304. (doi:10.1103/PhysRevE.84.051304)
36. Mandal S, Nicolas M, Poiliquen O. 2020 Insights into the rheology of cohesive granular media. *Proc. Natl Acad. Sci. USA* **117**, 8366–8373. (doi:10.1073/pnas.1921778117)
37. Mandal S, Nicolas M, Poiliquen O. 2021 Rheology of cohesive granular media: shear banding, hysteresis, and nonlocal effects. *Phys. Rev. X* **11**, 021017. (doi:10.1103/PhysRevX.11.021017)
38. Barker T, Rauter M, Maguire E, Johnson C, Gray J. 2021 Coupling rheology and segregation in granular flows. *J. Fluid Mech.* **909**, A22. (doi:10.1017/jfm.2020.973)
39. Vo T, Nezamabadi S, Mutabaruka P, Delenne JY, Radjai F. 2020 Additive rheology of complex granular flows. *Nat. Commun.* **11**, 1476. (doi:10.1038/s41467-020-15263-3)
40. Tapia F, Ichihara M, Pouliquen O, Guazzelli E. 2022 Viscous-inertial transition in dense granular suspension. (https://arxiv.org/abs/2202.10641)
41. Nicot F, Hadda N, Guessasma M, Fortin J, Millet O. 2013 On the definition of the stress tensor in granular media. *Int. J. Solids Struct.* **50**, 2508–2517. (doi:10.1016/j.ijsolstr.2013.04.001)
42. Yan B, Regueiro R. 2019 Definition and symmetry of averaged stress tensor in granular media and its 3D DEM inspection under static and dynamic conditions. *Int. J. Solids Struct.* **161**, 243–266. (doi:10.1016/j.ijsolstr.2018.11.021)
43. Luding S. 2010 Macroscopic stress from dynamic, rotating granular media. *Am. Inst. Phys. Conf. Proc.* **1227**, 208–213. (doi:10.1063/1.3435391)
44. Shen H, Hibler III W, Leppäranta M. 1984 On the rheology of a broken ice field due to floe collision. *MIZEX Bulletin III, USACREL Special Report 84-28*, pp. 29–34.
45. Lu Q, Larsen J, Tryde P. 1989 On the role of ice interaction due to floe collisions in marginal ice zone dynamics. *J. Geophys. Res.* **94**, 14 525–14 537. (doi:10.1029/JC094iC10p14525)
46. Leppäranta M, Lensu M, Lu QM. 1989 Shear flow of sea ice in the marginal ice zone with collision rheology. *Geophysica* **25**, 57–74.
47. Goldhirsch I. 1999 Scales and kinetics of granular flows. *Chaos* **9**, 659–672. (doi:10.1063/1.166440)
48. Yulmetov R, Lubbad R, Løset S. 2016 Planar multi-body model of iceberg free drift and towing in broken ice. *Cold Regions Sci. Technol.* **121**, 154–166. (doi:10.1016/j.coldregions.2015.08.011)
49. Li H, Lubbad R. 2018 Laboratory study of ice floes collisions under wave action. In *Proc. 28th Int. Ocean and Polar Engng Conf. ISOPE-2018, Sapporo, Japan, 10–15 June 2018*.
50. Haff PK. 1983 Grain flow as a fluid-mechanical phenomenon. *J. Fluid Mech.* **134**, 401–430. (doi:10.1017/S0022112083003419)
51. Savage SB. 1998 Analyses of slow high-concentration flows of granular materials. *J. Fluid Mech.* **377**, 1–26. (doi:10.1017/S0022112098002936)
52. Herman A. 2016 Discrete-element bonded-particle Sea Ice model DESIgn, version 1.3a—model description and implementation. *Geosci. Model Dev.* **9**, 1219–1241. (doi:10.5194/gmd-9-1219-2016)
53. Babić M, Shen H. 1990 The stress tensor in granular shear flows of uniform, deformable disks at high solids concentration. *J. Fluid Mech.* **219**, 81–118. (doi:10.1017/S0022112090002877)
54. Voivret C, Radjaï F, Delenne JY, El Youssoufi MS. 2009 Multiscale force networks in highly polydisperse granular media. *Phys. Rev. Lett.* **102**, 178001. (doi:10.1103/PhysRevLett.102.178001)
55. Clauset A, Shalizi C, Newman M. 2009 Power-law distributions in empirical data. *SIAM Rev.* **51**, 661–703. (doi:10.1137/070710111)
56. Azéma E, Linero S, Estrada N, Lizcano A. 2017 Shear strength and microstructure of polydisperse packings: the effect of size span and shape of particle size distribution. *Phys. Rev. E* **96**, 022902. (doi:10.1103/PhysRevE.96.022902)

57. Cantor D, Azéma E, Sornay P, Radjai F. 2018 Rheology and structure of polydisperse three-dimensional packings of spheres. *Phys. Rev. E* **98**, 052910. (doi:10.1103/PhysRevE.98.052910)
58. Tan ML, Goldhirsch I. 1998 Rapid granular flows as mesoscopic systems. *Phys. Rev. Lett.* **81**, 3022–3025. (doi:10.1103/PhysRevLett.81.3022)
59. Goldhirsch I. 2001 Granular gases: probing the boundaries of hydrodynamics. In *Granular gases* (eds T Pöschel, H Luding), pp. 79–99. Berlin, Germany: Springer Int.
60. van den Berg M, Lubbad R, Løset S. 2019 The effect of ice floe shape on the load experienced by vertical-sided structures interacting with a broken ice field. *Mar. Struct.* **65**, 229–248. (doi:10.1016/j.marstruc.2019.01.011)
61. Nguyen DH, Azéma E, Radjai F, Sornay P. 2014 Effect of size polydispersity versus particle shape in dense granular media. *Phys. Rev. E* **90**, 012202. (doi:10.1103/PhysRevE.90.012202)
62. Nguyen DH, Azéma E, Sornay P, Radjai F. 2015 Effects of shape and size polydispersity on strength properties of granular materials. *Phys. Rev. E* **91**, 032203. (doi:10.1103/PhysRevE.90.032203)
63. Herman A, Wenta M, Cheng S. 2021 Sizes and shapes of sea ice floes broken by waves-a case study from the East Antarctic coast. *Front. Earth Sci.* **9**, 655977. (doi:10.3389/feart.2021.655977)